

# Minimal design of a synthetic cilium

Clément Moreau,<sup>1,2,\*</sup> Benjamin J. Walker,<sup>3,4,†</sup> Rebecca N. Poon,<sup>5</sup> Daniel Soto,<sup>6</sup> Daniel I. Goldman,<sup>6</sup> Eamonn A. Gaffney,<sup>7,‡</sup> and Kirsty Y. Wan<sup>5,§</sup>

<sup>1</sup>*Nantes Université, École Centrale Nantes, CNRS, LS2N, UMR 6004, F-44000 Nantes, France*

<sup>2</sup>*Research Institute for Mathematical Sciences, Kyoto University, Kyoto, 606-8502, Japan*

<sup>3</sup>*Department of Mathematical Sciences, University of Bath, Bath, BA2 7AY, UK*

<sup>4</sup>*Department of Mathematics, University College London, London, WC1E 6BT, UK*

<sup>5</sup>*Living Systems Institute & Department of Mathematics and Statistics,*

*University of Exeter, Exeter EX4 4QD, United Kingdom*

<sup>6</sup>*School of Physics, Georgia Institute of Technology, Atlanta, GA 30332, United States of America*

<sup>7</sup>*Mathematical Institute, University of Oxford, Oxford, OX2 6GG, United Kingdom*

(Dated: December 11, 2024)

We study a slender filament beating in a viscous fluid with novel curvature-dependent bending stiffness. Our numerical and experimental investigations reveal that such differential stiffness can sustain planar bending waves far along flexible filaments, in stark contrast to the uniform-stiffness case which requires more sophisticated control. In particular, we establish basal actuation as a viable, parsimonious mechanism for generating high-amplitude planar bending waves. Moreover, the resulting beat patterns closely resemble the power-and-recovery strokes of propulsive biological filaments such as cilia, suggesting extensive applications in robotic and engineered systems.

## INTRODUCTION

The cilium is a complex, highly conserved organelle found in diverse organisms where it contributes to a host of important functions, including flow manipulation and self-propulsion of microorganisms [1, 2]. Inspired by these natural capabilities, there has been significant interest and progress in the field in fabricating micro or even nanoscopic devices that can also be used to enable fluid pumping, swimming, particle mixing and manipulation. Synthetic systems are currently unable to match the versatility of biological cilia, which has driven the development of sophisticated artificial control mechanisms. Magnetic actuation has become the favoured strategy to precisely engineer realistic beat patterns in ensembles of artificial cilia, though many other methods have been employed, including pneumatic, electrochemical, and optical actuation [3, 4]. Rather than devise increasingly sophisticated modalities of control, we consider an alternative approach: is it possible to engineer the material properties of a filament to produce realistic, cilia-like beat patterns using only a simple control mechanism?

To explore this idea, we revisit a seminal study of the fluid-structure interactions of a swimming mammalian spermatozoan, Fig. 1a from the 1950s. Here, Machin contrasted two popular competing hypotheses of the time [7]: (1) the filament is driven from the base (at its interface with the cell body) but is otherwise passive, and (2) it is driven by active elements along its length. Through a theoretical analysis of an idealised Euler elastica in the absence of inertia, Machin concluded that passive, proximally driven filaments were incapable of reproducing large-amplitude bending waves that are characteristic of eukaryotic cilia and flagella [2, 8, 9]. In particular, Machin noted that, depending on parameters, one of two

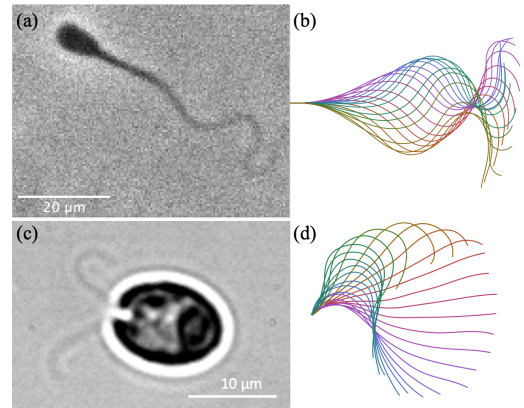


FIG. 1. Examples of flagellar actuation in biological microswimmers. Beating flagella of (a) a bovine spermatozoon and (c) *Chlamydomonas reinhardtii* display large amplitude bending at their distal ends. (b,d) Traces of the waveforms, color-coded in time, highlight the symmetric beat pattern for the sperm cell and marked asymmetry in *Chlamydomonas* between the power and recovery strokes. Images (a,b), (c,d) are reproduced with permission from Walker *et al.* [5] and Wan and Goldstein [6], respectively.

things occurred: (1) the amplitude of bending waves decayed rapidly along the flagellum, so that distal amplitudes were effectively negligible (Fig 3 F-J of [7]), or (2) bending only occurred with long wavelength, with fewer than approximately 1.5 wavelengths being present along the flagellum (Fig 3 A-E of [7]).

Machin's study refuted the first of the two hypotheses for flagellar beating, a result later confirmed by experiments that culminated in the identification of spatially distributed dynein as the molecular motors responsible for force generation inside these filaments [10–12]. As

these filaments are remarkably conserved across eukaryotes ([1, 11, 13, 14] and Fig. 1), it is now well-established that ciliary beating is universally driven by distributed activity rather than localised actuation. Indeed, cilia completely isolated from the cell body continue to beat in the presence of ATP [15–17]. Hence, proximal actuation has been duly passed over as a driver of motility in eukaryotic systems. This notably contrasts with flagellated bacteria and archaea, which self-propel using a rotary motor that generates basal torque to spin a helical flagellum [18, 19].

Thus, the prospect of driving cilia-like beating patterns in elastic filaments via basal actuation alone would appear to be unrealistic. However, while the material properties of biological cilia and flagella are restricted by developmental or evolutionary constraints, engineered synthetic filaments may be designed with more freedom [3, 20–22]. This raises a simple question: by modifying the mechanical properties of a filament, can the conclusions of Machin’s analysis be sidestepped? Can we produce realistic bending waves in engineered passive filaments for low-Reynolds number propulsion using only basal actuation? If so, this simple mechanism would facilitate the development of markedly simple synthetic systems without intricate mechanisms of distributed driving or control. In turn, these may be designed to exploit asymmetric ciliary beating either for propulsion, such as in multi-ciliated swimmers like *Chlamydomonas*, or for flow generation, as observed in epithelial cilia. This strategy is analogous to implementing directional compliance in robotic appendages modelled upon the limbs of insects [23], the undulatory motion of snakes [24] or magnetic metamaterials [25–27], which can greatly reduce the costs of gait computation.

Seeking to embody novel functionality within simple synthetic systems, we combine theoretical study with a novel engineered physical system. In this Letter we establish how sustained, cilia-like beating patterns can be driven by basal actuation alone in appropriately designed filaments.

### MACHIN’S LOW-AMPLITUDE MODEL

To motivate our eventual design principle, we consider (following [7]) the propagation of bending waves along an elastic filament in a fluid using the dimensionless small-amplitude beam equation

$$\frac{\partial y}{\partial t} = -\frac{\partial^2}{\partial x^2} \left( E \frac{\partial^2 y}{\partial x^2} \right) \quad (1)$$

with boundary conditions

$$y(0, t) = 0, \quad \frac{\partial y}{\partial x}(0, t) = A \sin t, \quad (2a)$$

$$\frac{\partial^2 y}{\partial x^2}(1, t) = 0, \quad \frac{\partial^3 y}{\partial x^3}(1, t) = 0. \quad (2b)$$

This system corresponds to a filament with displacement  $y$  driven by rotation about a hinge at  $x = 0$ , with moment-free and shear-free conditions at the tip  $x = 1$ . Throughout, we use dimensionless quantities such that  $E$  captures the ratio of bending resistance to drag, the driving oscillations occur at unit frequency, and the filament is of unit length. Balancing terms in Eq. (1) gives rise to a natural dimensionless lengthscale  $l \propto \sqrt[4]{E}$ , over which planar elastic waves decay exponentially.

Many studies have generalised Machin’s model, going beyond the small-amplitude limit and into three dimensions [28–31], or have considered hydrodynamic and basal synchronisation of several flagella [32, 33], follower force actuation [34] or non-uniform, spatially-varying stiffness [35, 36]. Here, we seek an alternative generalisation and incorporate state dependence into the stiffness, setting  $E = E(\frac{\partial^2 y}{\partial x^2})$  to depend on the local linearised curvature. For simplicity, we consider  $E$  to be piecewise constant, so that

$$E(\kappa) = \begin{cases} E_L & \text{if } \kappa > 0, \\ E_R & \text{if } \kappa \leq 0 \end{cases} \quad (3)$$

for unequal constants  $E_L > E_R > 0$  and curvature  $\kappa \in \mathbb{R}$ . Solving Eq. (1) is now somewhat involved, but we can estimate the appropriate decay lengthscale by considering a further simplification.

Suppose that, instantaneously, the filament is divided into two equal regions of positive and negative curvature, similar to a sinusoid over a single period. Up to constants and over a fixed timescale, the appropriate decay lengthscale in the region of positive curvature is  $l_L = \sqrt[4]{E_L}$ ; in the region of negative curvature, the decay lengthscale is  $l_R = \sqrt[4]{E_R}$ . Note  $l_L > l_R$ . Hence, the amplitude of planar bending waves after passing through both regions experiences decay scaling with  $\exp(-\frac{1}{2}[1/l_L + 1/l_R])$ , as opposed to either of  $\exp(-1/l_L)$  and  $\exp(-1/l_R)$ . Hence, there is an effective decay lengthscale of  $2(1/l_L + 1/l_R)^{-1}$  in the filament, equal to the harmonic mean of the two individual lengthscales of decay. Notably, this is at least as large as the smallest lengthscale  $l_R$ , and approaches  $2l_R$  as  $E_L \rightarrow \infty$ . Intuitively, this latter case corresponds to a filament that is extremely hard to bend in one direction, whilst being relatively compliant in the other.

This reasoning readily generalises to filaments where a proportion  $\alpha \in (0, 1)$  is bent such that  $E = E_R$ . In this case, the effective lengthscale is  $([1 - \alpha]/l_L + \alpha/l_R)^{-1}$ , which approaches  $l_R/\alpha > l_R$  as  $E_L \rightarrow \infty$ . Whilst clearly  $\alpha$  should not be considered to be a fixed quantity in a

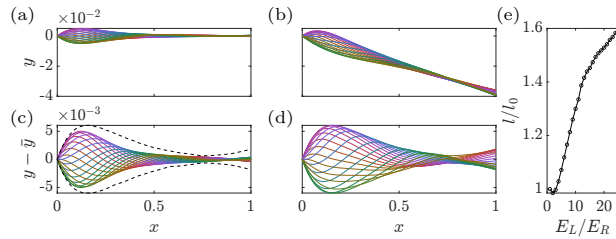


FIG. 2. Differential stiffness and small-amplitude beating. (a,b) Computed solutions of the small-amplitude beam equation over time with (a)  $E_L = E_R = 10^{-4}$  and (b)  $E_L = 10^{-3}$ ,  $E_R = 10^{-4}$ . (c,d) Deviation from the average configuration  $\bar{y}$ , highlighting increased amplitude with differential filament stiffness. The envelope of (d) is overlaid on (c) as black dashed curves. (e) Estimated decay lengthscale  $l$  as a function of differential stiffness, relative to the lengthscale  $l_0$  in the equal-stiffness case. Here,  $A = 0.1$ .

dynamic filament, this back-of-the-envelope scaling analysis suggests that state-dependent bending stiffness could greatly enhance the effective decay length, with filaments thereby being able to transmit bending waves far along their lengths. Importantly, this mechanism unifies desirable properties of both high and low stiffness regimes: bending waves can be of high curvature (associated with the lower bending stiffness) and also propagate far along the filament (associated with the higher bending stiffness). Thus, filaments with differential stiffness are qualitatively different to their constant-stiffness counterparts.

To examine these idealised arguments thoroughly, a numerical study of filaments with differential bending stiffness is presented in Fig. 2, computed using FEniCS [37], wherein the state-dependent stiffness is taken to vary smoothly (but rapidly) between  $E_L$  and  $E_R$  (detailed in the Supplementary Material). We encourage readers to explore this system for themselves via a browser-based VisualPDE simulation [38]. The contrast between a uniform filament (a) and a filament with state-dependent stiffness (b) is marked, with the latter being highly asymmetric. The amplitude of distal motion is significantly greater in (b) than in (a), visible in the mean-centered plots of (c) and (d). This enhancement of both the distal amplitude and the apparent decay lengthscale agree qualitatively with the scaling analysis. This is further supported by numerical estimation of the decay lengthscale as a function of the degree of differential stiffness (Fig. 2e), described in the Supplementary Material. Thus, at least in the small-amplitude regime, state-dependent stiffness is a plausible mechanism for propagating planar bending waves along filaments.

## LARGE-AMPLITUDE BENDING

To investigate beyond the small-amplitude regime, we adopt a geometrically nonlinear framework [39, 40]. The

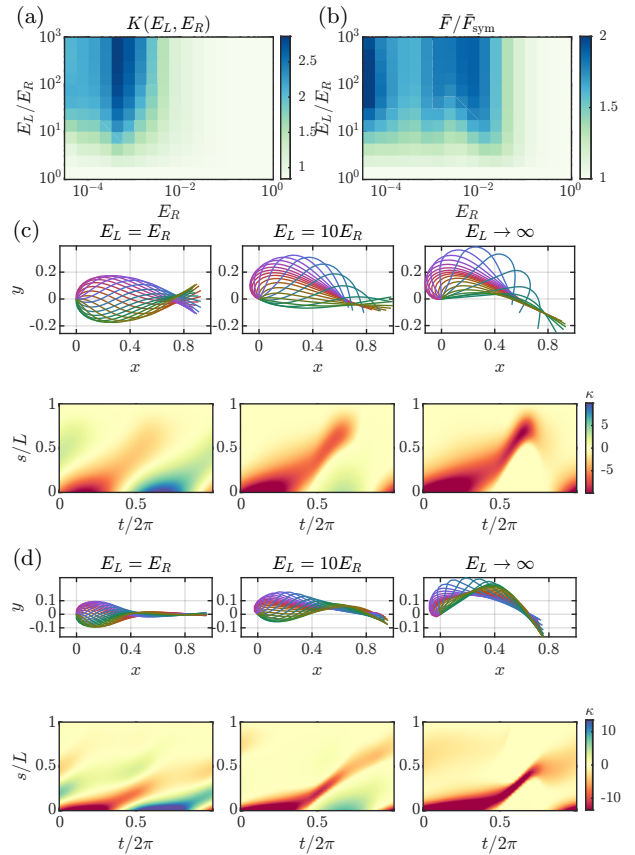


FIG. 3. Effects of differential stiffness in the geometrically nonlinear regime ( $A = \pi/2$ ), obtained from numerical solution of Eq. (4). (a,b) Relative increase in (a) maximal curvature and (b) average force at the pinned end, for a range of stiffnesses  $E_R$  and differential stiffnesses  $E_L/E_R$ . Example waveforms are shown below for (c) medium stiffness ( $E_R = 1.6 \times 10^{-3}$ ) and (d) low stiffness ( $E_R = 1 \times 10^{-4}$ ). (c,d) Example beating patterns (rotated in the beating plane to align horizontally) and associated curvature kymographs for filaments of (c) medium stiffness ( $E_R = 1.6 \times 10^{-3}$ ) and (d) low stiffness ( $E_R = 1 \times 10^{-4}$ ). From left to right: symmetric beating ( $E_L = E_R$ ), resembling the classical solution of Fig. 2; an intermediate case ( $E_L/E_R = 10$ ), matching that studied in the small-amplitude regime; and a highly asymmetric “locking” case ( $E_L/E_R = 10^3$ ), effectively forbidding negative curvatures.

analogue of Eq. (1) in the geometrically nonlinear regime is

$$E \frac{\partial \theta}{\partial s} + \int_s^1 [\mathbf{x}(\tilde{s}) - \mathbf{x}(s)] \times \mathbf{f}(\tilde{s}) d\tilde{s} = 0 \quad (4)$$

written in terms of the tangent angle  $\theta$  (measured relative to a fixed axis), position  $\mathbf{x} = (x, y)$ , and hydrodynamic drag  $\mathbf{f}$ , each functions of arclength  $s \in [0, 1]$  and dimensionless. The derivation of this integral equation and the underlying assumptions are described in

detail by Moreau *et al.* [39], recounted in part in the Supplementary Material. In the nonlinear regime, curvature is  $\kappa = \frac{\partial\theta}{\partial s}$ , so that  $E = E(\kappa)$ . Solving this integro-differential equation numerically (as described in the Supplementary Material) allows us to test the predictions of the linear theory well beyond its regime of validity. In the following, we set  $A = \pi/2$ .

In this general regime, a quantitative measure of the effects of stiffness is the relative increase in maximum curvature over one beating period, averaged over the flagellum, defined for given  $E_L$  and  $E_R$  as

$$K(E_L, E_R) = \int_0^1 \frac{\max_t |\kappa_{E_L, E_R}(s, t)|}{\max_t |\kappa_{E_R, E_R}(s, t)|} ds, \quad (5)$$

where the maximum over  $t$  is computed over one time period in the limiting periodic regime. Naturally,  $\kappa_{E_L, E_R}(s, t)$  and  $\kappa_{E_R, E_R}(s, t)$  refer to the curvature for the asymmetric and symmetric filaments, respectively.

This quantity is presented in panel (a) of Fig. 3, plotted as a function of  $E_R$  and the differential stiffness  $E_L/E_R$ , demonstrating that differential stiffness can greatly enhance the curvatures attained by a filament during a beating period. The relative increase is three-fold around  $E_R \approx 1 \times 10^{-3}$ .

To confirm that the increase in average curvature is localised towards the distal end of the filament, we also determined the maximum value  $K_{\max}$  and its argument  $s_{\max}$  over  $s \in [0, 1]$  of the integrand in Eq. (5), indicating where the qualitative change between uniform and differential stiffness is the greatest. For any value of  $E_L$  and  $E_R$ ,  $s_{\max}$  takes values between 0.5 and 0.8, confirming the trend in Fig. 3. Around  $E_R \approx 1 \times 10^{-3}$ , the corresponding value of  $K_{\max}$  goes up to 6, further highlighting the capacity of differential stiffness to transport and even amplify curvature for large beating amplitudes.

Machin identified (in the small-amplitude limit) that exponential decay significantly hinders planar wave propagation towards the distal end when the filament length exceeds five times the characteristic lengthscale  $\sqrt[3]{E_R}$ . Surprisingly, the parameter regime in which we see maximal curvature increase due to differential stiffness approximately corresponds to this case. Moreover, the curvature increase remains markedly high even when considering very small  $E_R$  ( $< 10^{-4}$ , representing a filament more than 10 times longer than the relaxation lengthscale), for which the effect of proximal actuation with uniform stiffness is virtually negligible at the distal end.

Figure 3b displays the magnitude  $\bar{F}$  of the pinning force, exerted on the point of attachment at the proximal end, averaged over one beating period, and normalised by the time-averaged force without differential stiffness,  $\bar{F}_{\text{sym}}$ . As should be expected, maintaining a prescribed actuation while increasing filament stiffness for positive curvature comes at the cost of increasing the average pinning force. However, this relative increase remains smaller than the relative curvature enhancement

through most values of  $E_R$  and  $E_L$ , indicating that differential stiffness constitutes an efficient way of increasing curvature according to this measure. For all values of  $E_L/E_R$ , the relative force  $\bar{F}/\bar{F}_{\text{sym}}$  has a local minimum with respect to  $E_R$  for  $E_R \approx 1.6 \times 10^{-3}$ . Simultaneously,  $K(E_L, E_R)$  is approximately maximal, so that the ratio between  $K(E_L, E_R)$  and  $\bar{F}/\bar{F}_{\text{sym}}$  is also approximately maximal. This value of  $E_R$  appears to be optimal for enhanced curvature generation with differential stiffness.

Panels (c) and (d) of Fig. 3 illustrate filament beats in the large amplitude regime for various degrees of differential stiffness. In the left column, we take  $E_L = E_R$  and reproduce the symmetric, short-lengthscale beating predicted by Machin’s low-amplitude analysis for differing baseline stiffness  $E_R$ . In the subsequent columns, increasing degrees of differential stiffness yield larger amplitude deviations at the distal end of the filament while also allowing for high-curvature planar bending waves to propagate. These beats are further represented in the plots of signed curvature  $\kappa$  beneath the beating patterns, from which the high curvatures of the asymmetric regimes are evident. The spatial extent of bending waves is also clearly visible, with differential stiffness giving rise to far-reaching bending. Moreover, in the case  $E_R \approx 1.6 \times 10^{-3}$  (Fig. 3c), the resulting beat patterns begin to resemble the *power-and-recovery strokes* typical of most cilia, including *Chlamydomonas* (Fig. 1d), other protists [41–43], and vertebrate respiratory cilia [44].

Thus, even beyond the small-amplitude regime, differential stiffness presents itself as an effective mechanism for enhancing elastic planar wave propagation.

## ENGINEERING CILIA-LIKE BEATING

Given the striking resemblance of the simulated beat of Fig. 3c with those seen in certain biological specimens, we now ask if we can realise biomimetic beating in practice using only basal actuation and differential stiffness? To explore this, we built a macroscopic robotic realisation of a basally actuated filament, schematised in Fig. 4a. The continuum limit is difficult to implement in practice, so our robotic filament comprises a finite number of links connected by custom hinges that are designed to qualitatively mimic differential stiffness [20].

These hinges, illustrated in Fig. 4b, are asymmetric in shape, so they only admit bending in one direction, similar to the “locking” limit  $E_L \gg E_R$  explored above. Each of the three links is 1.6 cm long, with a 1.2 cm basal attachment, so that the total length of the filament from its rotation point is 6 cm. The locking hinges are designed to reproduce the most extreme case of differential stiffness in the limit of  $E_L \gg E_R$  (as seen in Fig. 3c). Notably, these hinges are simple to customise and produce.

The filament is driven at the base by a XL430-W250 dynamixel motor, which rotates through  $180^\circ$  at an an-

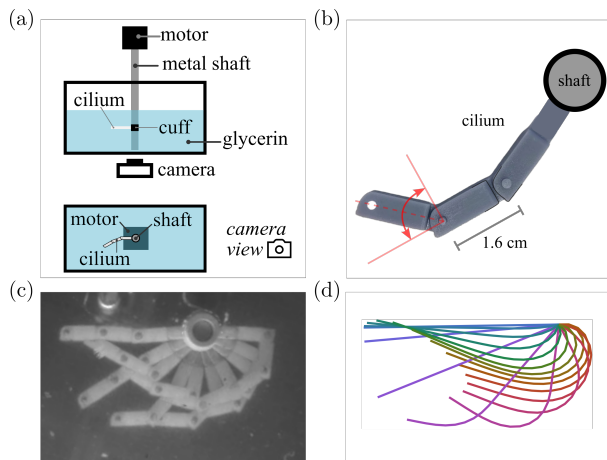


FIG. 4. Experimental realisation of differential stiffness in a bio-inspired macroscale robotic cilium (Supplementary Video 1). Motion is driven only by actuating the base of the filament. (a) Diagram of the experimental setup, not to scale. The cilium is placed in a tank of glycerin, and imaged from below. The cilium is connected to the driving motor by a vertical metal shaft. (b) Detail of the locking mechanism. The links are designed so that each link can rotate freely only within the  $90^\circ$  angle indicated in red. (c) Snapshots of the robotic filament overlaid in time compared to (d) a simulated waveform, with  $A = \pi/2$ ,  $E_R = 2 \times 10^{-3}$ ,  $E_L \gg E_R$  highlighting marked agreement between the synthetic and *in silico* systems.

gular velocity of  $5^\circ \text{s}^{-1}$ . To remain in the low-Reynolds regime, the filament is placed in a tank of glycerin, which has density of  $1.26 \times 10^3 \text{ kg m}^{-3}$  and viscosity  $1.4 \text{ Pa s}$ . The oscillatory Reynolds number  $\rho f L^2 / \eta = 0.3$ . Visual inspection of the beating filament confirmed that inertial coasting was negligible. The tank measures  $60 \text{ cm}$  by  $32 \text{ cm}$ , with depth  $18 \text{ cm}$ . The filament is positioned far from walls to minimise boundary interactions. Imaging was performed at  $1 \text{ Hz}$  using a Logitech webcam. The cilia were resin printed using an Anycubic Photon Mono X, in Anycubic resin, and density matched to the glycerin.

Prescribing a basal amplitude  $A = \pi/2$ , the beat pattern of the robotic filament is showcased in Fig. 4c. Even without elasticity, the power and recovery strokes are clearly distinguished, with experimental waveforms closely resembling the cilia-like beating observed in our nonlinear simulations (Fig. 4d). Further analysis, including a maximum intensity projection of the full video (Supplementary Video 1, 12 beat cycles in total), shows that small tracer particles in the fluid move a net distance of approximately  $0.1 \text{ cm}$  per beat cycle, evidencing net pumping of fluid by this artificial cilium. (See the Supplementary Material for details.) A full and faithful model of the robotic system and a complete parameter analysis will be explored in future study.

## SUMMARY AND CONCLUSIONS

Through a combination of experiments and theory, we have demonstrated that enhanced wave propagation can be achieved with marked simplicity, realising cilia-like beats in engineered filaments using basal actuation alone, contrasting for instance with distributed magnetic actuation in recent similar designs of robots with structural asymmetric stiffness [25, 27]. By incorporating a curvature-dependent stiffness we pragmatically generate biologically realistic planar waveforms using only a simple modality of control. This highlights and newly establishes the ready potential for simple, parsimonious synthetic systems to reproduce this well-studied, broadly applicable and widely conserved biological phenomenon. More generally, it paves the way for new avenues of multidisciplinary enquiry into the motility and actuation of synthetic systems at the microscale.

It is well known that mammalian sperm flagella have a spatially heterogeneous bending stiffness with higher proximal stiffness [45, 46]. This is potentially analogous to the larger initial link in the macroscale robotic cilium depicted in Fig. 4b, which prevents proximal bending, and the functional impact of time-independent axisymmetric heterogeneity has been explored in a number of studies [47, 48]. However, biological cilia also possess numerous protein complexes positioned along axonemal microtubule arrays that could harbour *dynamic* structural heterogeneities that do not possess axisymmetry, contributing to an effective state-dependent stiffness [49–52]. The potential for dynamic tuning of apparent and state dependent bending stiffness in these structures has not been previously considered. Nonetheless, the dynamic modulation of these asymmetries in live cells, e.g. by phosphorylation, could contribute to the generation of distinct beat patterns on the same structure, noting that flagella stiffness changes with the level of ATP [53–55], which in turn has been associated with the extent of phosphorylation of outer dynein arm-linked proteins [56]. In particular, to achieve control systems for microscale movement, cells must exploit the mechanical or physical intelligence of their bodies, which could be realised, at least in part, through state-dependent bending stiffness of their cilia.

## ACKNOWLEDGEMENTS

This work was funded by the Japan Society for the Promotion of Science (Fellowship No. PE22023 and Grant No. 22KF0197 to C.M) and the Research Institute for Mathematical Sciences, an International Joint Usage/Research Center located at Kyoto University (C.M), by the Royal Commission for the Exhibition of 1851 (B.J.W), by the European Research Council under the European Union’s Horizon 2020 research and innovation

programme grant 853560 EvoMotion (K.Y.W), and a Company of Biologists travelling fellowship (R.N.P and K.Y.W).

For the purpose of Open Access, the author has applied a CC BY public copyright licence to any Author Accepted Manuscript (AAM) version arising from this submission.

- 
- \* clement.moreau@cnrs.fr  
† bjw43@bath.ac.uk  
‡ gaffney@maths.ox.ac.uk  
§ k.y.wan2@exeter.ac.uk
- [1] D. R. Mitchell, Evolution of cilia, Cold Spring Harbor Perspectives in Biology **9**, a028290 (2017).
  - [2] C. Brennen and H. Winet, Fluid-mechanics of propulsion by cilia and flagella, Ann. Rev. Fluid Mech. **9**, 339 (1977).
  - [3] T. ul Islam, Y. Wang, I. Aggarwal, Z. Cui, H. Es-lami Amirabadi, H. Garg, R. Kooi, B. B. Venkataramanachar, T. Wang, S. Zhang, P. R. Onck, and J. M. J. den Toonder, Microscopic artificial cilia – a review, Lab Chip **22**, 1650 (2022).
  - [4] H. Gu, Q. Boehler, H. Cui, E. Secchi, G. Savorana, C. De Marco, S. Gervasoni, Q. Peyron, T.-Y. Huang, S. Pane, A. M. Hirt, D. Ahmed, and B. J. Nelson, Magnetic cilia carpets with programmable metachronal waves, Nature Communications **11**, 2637 (2020).
  - [5] B. J. Walker, S. Phuyal, K. Ishimoto, C.-k. Tung, and E. A. Gaffney, Computer-assisted beat-pattern analysis and the flagellar waveforms of bovine spermatozoa, Royal Society Open Science **7**, 200769 (2020).
  - [6] K. Y. Wan and R. E. Goldstein, Rhythmicity, recurrence, and recovery of flagellar beating, Physical Review Letters **113** (2014).
  - [7] K. E. Machin, Wave propagation along flagella, J. Exp. Biol. **35**, 796 (1958).
  - [8] D. M. Woolley and G. G. Vernon, A study of helical and planar waves on sea urchin sperm flagella, with a theory of how they are generated, J. Exp. Biol. **204**, 1333 (2001).
  - [9] M. T. Gallagher, G. Cupples, E. H. Ooi, J. Kirkman-Brown, and D. Smith, Rapid sperm capture: high-throughput flagellar waveform analysis, Human Reproduction **34**, 1173 (2019).
  - [10] I. Gibbons, Studies on protein components of cilia from tetrahymena pyriformis, PNAS **50**, 1002 (1963).
  - [11] I. Gibbons and A. Rowe, Dynein - a protein with adenosine triphosphatase activity from cilia, SCIENCE **149**, 424 (1965).
  - [12] K. E. Summers and I. R. Gibbons, Adenosine triphosphate-induced sliding of tubules in trypsin-treated flagella of sea-urchin sperm, PNAS **68**, 3092 (1971).
  - [13] C. B. Lindemann, The flagellar germ-line hypothesis: How flagellate and ciliate gametes significantly shaped the evolution of organismal complexity, Bioessays **44**, 10.1002/bies.202100143 (2022).
  - [14] S. S. Merchant, S. E. Prochnik, O. Vallon, E. H. Harris, S. J. Karpowicz, G. B. Witman, A. Terry, A. Salamov, L. K. Fritz-Laylin, L. Marechal-Drouard, W. F. Marshall, L.-H. Qu, D. R. Nelson, A. A. Sanderfoot, M. H. Spalding, V. V. Kapitonov, Q. Ren, P. Ferris, E. Lindquist, H. Shapiro, S. M. Lucas, J. Grimwood, J. Schmutz, C. A. Team, I. V. JGI Annotation Team Grigoriev, D. S. Rokhsar, and A. R. Grossman, The chlamydomonas genome reveals the evolution of key animal and plant functions, Science **318**, 245 (2007).
  - [15] V. F. Geyer, J. Howard, and P. Sartori, Ciliary beating patterns map onto a low-dimensional behavioural space, Nature Physics **18**, 332 (2022).
  - [16] M. Bessen, R. B. Fay, and G. B. Witman, Calcium control of waveform in isolated flagellar axonemes of chlamydomonas, The Journal of Cell Biology **86**, 446 (1980).
  - [17] K. Y. Wan, The beat of isolated cilia, Nature Physics **18**, 234 (2022).
  - [18] H. C. Berg and R. A. Anderson, Bacteria swim by rotating their flagellar filaments, Nature **245**, 380 (1973).
  - [19] M. Beeby, J. L. Ferreira, P. Tripp, S.-V. Albers, and D. R. Mitchell, Propulsive nanomachines: the convergent evolution of archaella, flagella and cilia, FEMS microbiology reviews **44**, 253 (2020).
  - [20] K. Diaz, T. L. Robinson, Y. O. Aydin, E. Aydin, D. I. Goldman, and K. Y. Wan, A minimal robophysical model of quadriflagellate self-propulsion, Bioinspiration & Biomimetics **16**, 066001 (2021).
  - [21] S. Sareh, J. Rossiter, A. Conn, K. Drescher, and R. E. Goldstein, Swimming like algae: biomimetic soft artificial cilia, Journal of the Royal Society Interface **10**, 20120666 (2013).
  - [22] S. Lim, Y. Du, Y. Lee, S. K. Panda, D. Tong, and M. Khalid Jawed, Fabrication, control, and modeling of robots inspired by flagella and cilia, Bioinspiration & Biomimetics **18**, 011003 (2023).
  - [23] J. C. Spagna, D. I. Goldman, P.-C. Lin, D. E. Koditschek, and R. J. Full, Distributed mechanical feedback in arthropods and robots simplifies control of rapid running on challenging terrain, Bioinspiration & biomimetics **2**, 9 (2007).
  - [24] T. Wang, J. Whitman, M. Travers, and H. Choset, Directional compliance in obstacle-aided navigation for snake robots, in *2020 American Control Conference (ACC) (IEEE, 2020)* pp. 2458–2463.
  - [25] S. Wu, Q. Ze, R. Zhang, N. Hu, Y. Cheng, F. Yang, and R. Zhao, Symmetry-breaking actuation mechanism for soft robotics and active metamaterials, ACS applied materials & interfaces **11**, 41649 (2019).
  - [26] N. Obayashi, A. Vicari, K. Junge, K. Shakir, and J. Hughes, Control and morphology optimization of passive asymmetric structures for robotic swimming, IEEE Robotics and Automation Letters **8**, 1495 (2023).
  - [27] M. Mohaghar, A. A. Connor, S. Wu, R. R. Zhao, and D. R. Webster, Effects of symmetry-breaking mechanisms on the flow field around magnetic-responsive material appendages that mimic swimming strokes, Physical Review Fluids **9**, 023101 (2024).
  - [28] C. J. Brokaw, Effects of increased viscosity on the movements of some invertebrate spermatozoa, J. Exp. Biol. **45**, 113 (1966).
  - [29] M. Hines and J. J. Blum, Bend propagation in flagella I. Derivation of equations of motion and their simulation, Biophys. J. **23**, 41 (1978).
  - [30] S. Camalet and F. Julicher, Generic aspects of axonemal beating, New J. Phys. **2**, 24.1 (2000).
  - [31] B. Rallabandi, Q. Wang, and M. Potomkin, Self-sustained three-dimensional beating of a model eukaryotic flagellum, Soft Matter **18**, 5312 (2022).

- [32] H. Guo, L. Fauci, M. Shelley, and E. Kanso, Bistability in the synchronization of actuated microfilaments, *Journal of Fluid Mechanics* **836**, 304 (2018).
- [33] H. Guo, Y. Man, K. Y. Wan, and E. Kanso, Intracellular coupling modulates biflagellar synchrony, *Journal of The Royal Society Interface* **18**, 20200660 (2021).
- [34] Y. Man and E. Kanso, Morphological transitions of axially-driven microfilaments, *Soft Matter* **15**, 5163 (2019).
- [35] Z. Peng, G. J. Elfring, and O. S. Pak, Maximizing propulsive thrust of a driven filament at low reynolds number via variable flexibility, *Soft Matter* **13**, 2339 (2017).
- [36] C. V. Neal, A. L. Hall-McNair, J. Kirkman-Brown, D. J. Smith, and M. T. Gallagher, Doing more with less: The flagellar end piece enhances the propulsive effectiveness of human spermatozoa, *Phys. Rev. Fluids* **5**, 073101 (2020).
- [37] A. Logg, K.-A. Mardal, and G. Wells, eds., *Automated Solution of Differential Equations by the Finite Element Method*, Lecture Notes in Computational Science and Engineering, Vol. 84 (Springer Berlin Heidelberg, Berlin, Heidelberg, 2012).
- [38] B. J. Walker, A. K. Townsend, A. K. Chudasama, and A. L. Krause, VisualPDE: rapid interactive simulations of partial differential equations, *Bulletin of Mathematical Biology* **85**, 113 (2023).
- [39] C. Moreau, L. Giraldi, and H. Gad elha, The asymptotic coarse-graining formulation of slender-rods, bio-filaments and flagella, *Journal of The Royal Society Interface* **15**, 20180235 (2018).
- [40] B. J. Walker, K. Ishimoto, H. Gadelha, and E. A. Gaffney, Filament mechanics in a half-space via regularised Stokeslet segments, *J. Fluid. Mech.* **879**, 808 (2019).
- [41] Z. Wang, T. Beneke, E. Gluenz, and R. J. Wheeler, The single flagellum of *Leishmania* has a fixed polarisation of its asymmetric beat, *Journal of Cell Science* **133**, jcs246637 (2020).
- [42] M. A. Sleight, Ciliary propulsion in protozoa, *Science Progress* (1933- ) **73**, 317 (1989).
- [43] H. Laeverenz-Schlogelhofer and K. Y. Wan, Bioelectric control of locomotor gaits in the walking ciliate euplotes, *Current Biology* (2024).
- [44] M. J. Sanderson and M. A. Sleight, Ciliary activity of cultured rabbit tracheal epithelium: beat pattern and metachrony, *Journal of Cell Science* **47**, 331 (1981).
- [45] K. A. Schmitz-Leisch and C. B. Lindemann, Direct measurement of the passive stiffness of rat sperm and implications to the mechanism of the calcium response, *Cell Motil. Cytoskel.* **59**, 169 (2004).
- [46] K. A. Leisch, D. W. Pelle, W. Dominic, and C. B. Lindemann, Insights into the mechanism of ADP action on flagellar motility derived from studies on bull sperm, *Biophys. J.* **95**, 472 (2008).
- [47] C. B. Lindemann, Functional significance of the outer dense fibers of mammalian sperm examined by computer simulations with the geometric clutch model, *Cell Motil. Cytoskel.* **34**, 258 (1996).
- [48] H. Gadelha and E. Gaffney, Flagellar ultrastructure suppresses buckling instabilities and enables mammalian sperm navigation in high-viscosity media, *J. R. Soc. Interface* **16**, 20180668 (2019).
- [49] K. H. Bui, T. Yagi, R. Yamamoto, R. Kamiya, and T. Ishikawa, Polarity and asymmetry in the arrangement of dynein and related structures in the chlamydomonas axoneme, *Journal of Cell Biology* **198**, 913 (2012).
- [50] S. K. Dutcher, Asymmetries in the cilia of chlamydomonas, *Philosophical Transactions of the Royal Society B* **375**, 20190153 (2020).
- [51] Z. Chen, G. A. Greenan, M. Shiozaki, Y. Liu, W. M. Skinner, X. Zhao, S. Zhao, R. Yan, Z. Yu, P. V. Lishko, *et al.*, In situ cryo-electron tomography reveals the asymmetric architecture of mammalian sperm axonemes, *Nature Structural & Molecular Biology* **30**, 360 (2023).
- [52] J. Lin and D. Nicastro, Asymmetric distribution and spatial switching of dynein activity generates ciliary motility, *Science* **360**, eaar1968 (2018), <https://www.science.org/doi/pdf/10.1126/science.aar1968>.
- [53] C. B. Lindemann, W. G. Rudd, and R. Rikmenspoel, The stiffness of the flagella of impaled bull sperm, *Biophysical Journal* **13**, 437 (1973).
- [54] M. Okuno and Y. Hiramoto, Direct measurements of the stiffness of echinoderm sperm flagella, *Journal of Experimental Biology* **79**, 235 (1979).
- [55] M. Okuno, Inhibition and relaxation of sea-urchin sperm flagella by vanadate, *J. Cell Biology* **85**, 712 (1980).
- [56] A. Yoshimura, I. Nakano, and C. Shingyoji, Inhibition by atp and activation by adp in the regulation of flagellar movement in sea urchin sperm, *Cell Motility And The Cytoskeleton* **64**, 777 (2007).

# Minimal design of a synthetic cilium

## Supplementary Material

Clément Moreau, Benjamin J. Walker, Rebecca N. Poon, Daniel Soto,  
Daniel I. Goldman, Eamonn A. Gaffney, Kirsty Y. Wan

### 1 Numerical methods

#### 1.1 Low-amplitude model

We seek to numerically solve the low-amplitude beam equation

$$\frac{\partial y}{\partial t} = -\frac{\partial^2}{\partial x^2} \left( E \frac{\partial^2 y}{\partial x^2} \right) \quad (1)$$

with boundary conditions

$$y(0) = 0, \quad \frac{\partial y}{\partial x}(0) = A \sin t, \quad (2a)$$

$$\frac{\partial^2 y}{\partial x^2}(1) = 0, \quad \frac{\partial^3 y}{\partial x^3}(1) = 0, \quad (2b)$$

where  $E = E(\frac{\partial^2 y}{\partial x^2})$  depends on the linearised curvature. We take the functional form of  $E$  to be a smooth function that rapidly transitions between unequal constants  $E_L > E_R > 0$ , specifically

$$E(\sigma) = E_R + \frac{[E_L - E_R][1 + \tanh(\sigma/\epsilon)]}{2} \quad (3)$$

for  $\epsilon = 0.1$ , which captures rapid transition over relevant curvatures. This PDE is solved in weak form using FEniCS [4] with adaptive implicit Euler timestepping and Lagrange elements. Source code is freely available at <https://github.com/Mar5bar/state-dependent-stiffness>.

An estimate for the decay lengthscale is computed from the numerical solutions as follows: for each discretised  $x \in [0.2, 0.6]$ , we computed the maximum absolute displacement from the temporal mean, with the limited range reducing the impact of end effects. These measurements of amplitude were fitted to an exponential of the form  $ce^{-x/l}$  using a logarithmic transformation and a linear-least-squares residual, yielding an estimate for the decay lengthscale  $l$ .

#### 1.2 VisualPDE simulation

The same equations as above are solved using VisualPDE.com via the numerical scheme described in [9], though with parameters adjusted to aid visualisation. Note that this simulation is intended only to provide a qualitative analogue of the high accuracy simulations of the previous section.

#### 1.3 Large-amplitude model

The development of the large-amplitude modelling framework is very similar to that of Hall-McNair et al. [2], Walker et al. [8], Walker and Gaffney [7] and especially Moreau et al. [5], which approximate a continuous elastic filament by a collection of links in a coarse graining of continuum elasticity. We modify the formulation of Moreau et al. [5] to include an actuated base and a state-dependent stiffness following eq. (3), but otherwise precisely adopt their methodology. We direct the interested reader to the noted publications for a full account of the approach, including the constitutive assumptions, and summarise it briefly below.

Moreau et al.'s approach discretises the beam into  $N$  straight segments of equal length and tracks the evolution of the orientation of each of these segments over time, relaxing the low-amplitude constraint inherent



in the above formulation. The governing equations remain those of moment balance, with the curvature captured as  $\frac{\partial\theta}{\partial s}$  in place of  $\frac{\partial^2 y}{\partial x^2}$  in the geometrically nonlinear regime. Explicitly, the dimensional analogue of eq. (1) is

$$E \frac{\partial\theta}{\partial s} + \int_s^1 [\mathbf{x}(\tilde{s}) - \mathbf{x}(s)] \times \mathbf{f}(\tilde{s}) d\tilde{s} = 0, \quad (4)$$

where  $\mathbf{f}(s)$  is the hydrodynamic drag associated with the motion at arclength  $s$  and  $E = E(\frac{\partial\theta}{\partial s})$ . The drag is related to the motion of the filament via the resistive force theory of Gray and Hancock [1], Hancock [3], which reads

$$\mathbf{f} = -C_N(\dot{\mathbf{x}} \cdot \mathbf{e}_N)\mathbf{e}_N - C_T(\dot{\mathbf{x}} \cdot \mathbf{e}_T)\mathbf{e}_T. \quad (5)$$

Here,  $\mathbf{e}_T(s)$  and  $\mathbf{e}_N(s)$  are unit tangent and normal vectors to the filament and  $\dot{\mathbf{x}}(s)$  is the velocity of a material point on the filament as measured in the laboratory frame. The positive constants  $C_T$  and  $C_N$  capture the magnitudes of hydrodynamic drag in the tangential and normal directions, respectively, and satisfy  $C_N/C_T = 2$ .

To proceed numerically, eq. (4) is applied at discrete arclengths  $s_i = iL/N$  for  $i \in \{0, \dots, N-1\}$ . Noting that the position  $\mathbf{x}(s_i)$  can be written solely in terms of the base  $\mathbf{x}(0)$  ( $\mathbf{0}$  without loss of generality) and the segment orientations  $\theta_i = \theta(s_i)$ , this generates a closed system of  $N$  ordinary differential equations in the unknown  $\theta_i$ . These equations are solved numerically in MATLAB [6] to yield the filament motion, utilising adaptive implicit timestepping with error tolerances set below  $10^{-6}$ . More concretely, the equations can be summarised in dimensionless form as

$$\text{Sp}^4 \mathbf{M} \dot{\boldsymbol{\theta}} = \mathbf{R}, \quad (6)$$

where  $\mathbf{M}$  is an invertible linear operator,  $\dot{\boldsymbol{\theta}}$  is the time derivative of the vector of the unknown  $\theta_i$ , and  $\mathbf{R}$  encodes the contribution of the state-dependent bending moments. The explicit and somewhat intricate form of these terms is given by Moreau et al. [5], Walker et al. [8]. Here, having implicitly non-dimensionalised, Sp is the governing dimensionless elastohydrodynamic parameter (the so-called *sperm number*), defined via

$$\text{Sp}^4 = \frac{C_N L^4}{E_m I T} \quad (7)$$

for typical bending modulus scale  $E_m$ , moment of inertia  $I$ , filament length  $L$ , and oscillation timescale  $T$ . In general, small Sp correspond to stiff filaments, whilst large Sp bend more readily in the fluid medium. In our study, we use a dimensionless parameter  $E_R$  which is related to the sperm number via  $\text{Sp} = E_R^{-1/4}$ . In particular, the value  $E_R = 10^{-4}$  used for the low-amplitude analysis corresponds to  $\text{Sp} = 10$ .

## 2 Net fluid pumping by a robotic cilium

Supplementary Video 1 shows 12 beat cycles of the robotic cilium beating in a tank of glycerin. The presence of small waste particles of cured resin in the tank allows the flow to be traced in certain locations. As we are interested in the average pumping rate, we perform a maximum intensity projection of the video, Fig 1, so that the paths of the ‘tracer particles’ show up as streaks. Visual inspection of the video confirms that the net movement of the tracers is in the same direction as the ciliary power stroke. The focal plane is sufficiently deep that many of the tracer particles are in the plane either above or below the beat plane of the robotic cilium. The strongest flow will be in the cilium beat plane, so we measure one of the longer tracer paths for this calculation, on the assumption that it is close to the beat plane. Over the 12 cycles of the video, this particle travels a net distance of 1.2 cm, giving an average net flow speed of 0.1 cm per beat cycle.

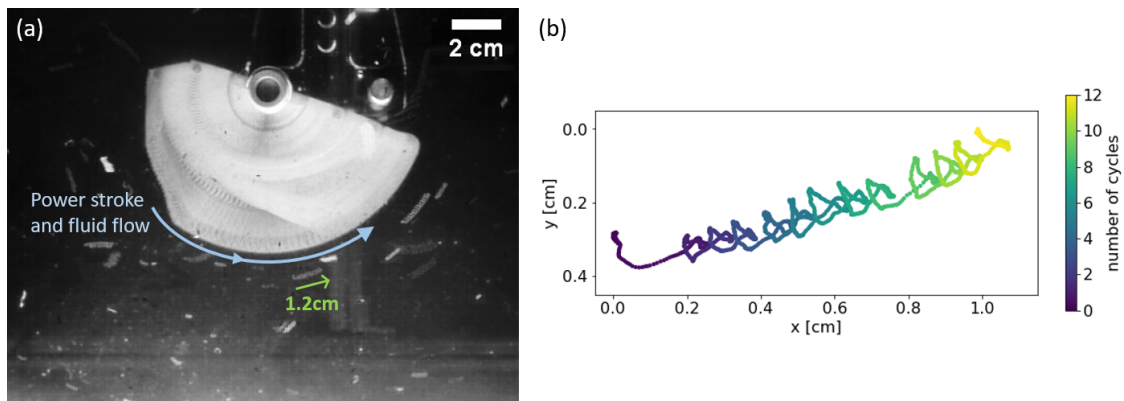


Figure 1: (a) A maximum intensity projection of Supplementary Video 1, showing 12 beat cycles. The paths of the ‘tracer particles’ can be seen as white streaks. The tracer particle annotated by a green arrow moves a total distance of 1.2 cm over the course of the video, so that the net flow speed is 0.1 cm per beat cycle. (b) Detailed position of the annotated particle throughout the video, colour coded by time.

## References

- [1] J. Gray and G. J. Hancock. The propulsion of sea urchin spermatozoa. *J. Exp. Biol.*, 32:802–814, 1955.
- [2] A. L. Hall-McNair, M. T. Gallagher, T. D. Montenegro-Johnson, H. Gadêlha, and D. J. Smith. Efficient Implementation of Elastohydrodynamics via Integral Operators. *Phys. Rev. Fluids.*, (4):1–24, 2019.
- [3] G. J. Hancock. The self-propulsion of microscopic organisms through liquids. *Proc. R. Soc. Lond. A*, 217: 96–121, 1953.
- [4] A. Logg, K.-A. Mardal, and G. Wells, editors. *Automated Solution of Differential Equations by the Finite Element Method*, volume 84 of *Lecture Notes in Computational Science and Engineering*. Springer Berlin Heidelberg, Berlin, Heidelberg, 2012. ISBN 978-3-642-23098-1. doi: 10.1007/978-3-642-23099-8. URL <https://link.springer.com/10.1007/978-3-642-23099-8>.
- [5] C. Moreau, L. Giralardi, and H. Gadêlha. The asymptotic coarse-graining formulation of slender-rods, bio-filaments and flagella. *Journal of The Royal Society Interface*, 15(144):20180235, 7 2018.
- [6] L. F. Shampine and M. W. Reichelt. The MATLAB ODE Suite. *SIAM Journal on Scientific Computing*, 18(1):1–22, jan 1997. ISSN 1064-8275. doi: 10.1137/S1064827594276424. URL <http://epubs.siam.org/doi/10.1137/S1064827594276424>.
- [7] B. Walker and E. Gaffney. Regularised non-uniform segments and efficient no-slip elastohydrodynamics. *Journal of Fluid Mechanics*, 915:A51, 5 2021.
- [8] B. J. Walker, K. Ishimoto, H. Gadelha, and E. A. Gaffney. Filament mechanics in a half-space via regularised Stokeslet segments. *J. Fluid. Mech.*, 879:808–873, 2019.
- [9] B. J. Walker, A. K. Townsend, A. K. Chudasama, and A. L. Krause. VisualPDE: rapid interactive simulations of partial differential equations. *Bulletin of Mathematical Biology*, 85(11):113, 2023.